Correspondence to:
N. Lahaye
noe.lahaye@inria.fr

Internal Tide Cycle and Topographic Scattering Over the North Mid-Atlantic Ridge

Noé Lahaye[1,2] , **Jonathan Gula[1]** , and **Guillaume Roullet[1]**

[1]Univ Brest, CNRS, Ifremer, IRD, Laboratoire d'Océanographie Physique et Spatiale (LOPS), IUEM, Plouzané, France, [2]Inria/Irmar, Campus Universitaire de Beaulieu, Rennes, France

Abstract Internal tides are a predominant source of high-frequency variability and diapycnal mixing in the ocean. Understanding their dynamics and lifecycle is necessary to better understand their role in the ocean circulation. In this study, we describe and quantify internal tide generation, propagation, and dissipation in a sector of the North Mid-Atlantic Ridge, using high-resolution numerical simulations with realistic bathymetry and stratification. We show that the generation and dissipation of internal tides, as well as the distribution of internal tides among vertical modes, exhibit high spatial variability. We find that topographic scattering leads to a significant transfer of energy toward high vertical modes and thereby enhances internal tide dissipation. On average, and especially on the ridge, this mechanism is dominant over the conversion from the barotropic tide for transferring energy to high (>7) vertical modes. The magnitude of the scattering of the first baroclinic internal mode is found to be in good agreement with theoretical predictions.

Plain Language Summary Internal waves are dynamical perturbations propagating throughout the stratified ocean. The internal waves generated by the interaction of the astronomical tide with the seafloor, the so-called "internal tides," are ubiquitous in the ocean. They are a predominant source of high-frequency variability and mixing. Understanding their dynamics and lifecycle is necessary to better understand their role in the ocean circulation. Here, we describe and quantify the internal tides generation, propagation and dissipation in a sector of the North Mid-Atlantic Ridge, using high-resolution numerical simulations with realistic bathymetry and stratification. We find that the interaction of the internal tide with the topography, leading to topographic scattering, is an important mechanism for dissipating internal tides energy.

1. Introduction

Internal tides are a key component of the ocean circulation. They are responsible for a large portion of the diapycnal mixing in the deep ocean (Kunze, 2017b; Polzin et al., 1997). Thereby, they greatly impact the large scale circulation (Kunze, 2017a; Melet et al., 2012) as well as vertical fluxes of nutrients in some regions—in particular near the surface (Sharples et al., 2009; Tuerena et al., 2019). They also contribute significantly to coastal shelf dynamics, where they have large amplitude and variability associated with nonlinear effects (Franks et al., 2019; Lamb, 2014; Nash et al., 2012; Pairaud et al., 2010). More indirectly, internal tides contaminate in situ observations (Hennon et al., 2019) as well as remote observations of the ocean such as satellite altimeter data. This has major implications, especially for the exploitation of data expected from the pending surface water and ocean topography mission (Morrow et al., 2019): internal tides alias the (sub)-mesoscale (Qiu et al., 2017; Torres et al., 2018) signature on sea surface height, thus making even more challenging the inversion of balanced current from such measurements (Ponte et al., 2017).

Studies of ocean internal tides started decades ago (Baines, 1973; Bell, 1975; Garrett & Kunze, 2007; Wunsch, 1975) and the subject has received growing attention ever since. It has been shown that numerous mechanisms impact internal tide dynamics. The major mechanisms include (Eden & Olbers, 2014; Müller et al., 1986; Polzin & Lvov, 2011): (1) interaction with (sub)-mesoscale ocean turbulence (Duda et al., 2018; Dunphy et al., 2017; Kafiabad et al., 2019; Savva & Vanneste, 2018), (2) scattering by topographic corrugations (Baines, 1971a; Kelly et al., 2013; Müller & Xu, 1992), and (3) nonlinear wave-wave interactions such as Parametric Subharmonic Instability (e.g., McComas & Bretherton, 1977; MacKinnon et al., 2012; D. J. Olbers, 1976; D. Olbers et al., 2020; Onuki & Hibiya, 2018). As low mode internal tides (typically the first and,

to a weaker extent, the second baroclinic modes) can propagate long distances, they lose coherence (which is associated with departure from an exactly repeating signal) through the above-mentioned processes (Buijsman et al., 2017; B. Li et al., 2020; Nelson et al., 2019) and, in addition, they have a remote impact in the ocean. This greatly complicates the spatial distribution of the internal tide field and its impact in the global ocean, and in particular the distribution of the associated diapycnal mixing (Melet et al., 2016). Such complexity constitutes one of the main challenges for capturing and developing efficient parameterization for global ocean circulation model of internal tide induced mixing (MacKinnon et al., 2017). Correspondingly, recently proposed parameterizations have incorporated simplified models of the propagation of the internal tide in order to improve the distribution of dissipation (Eden & Olbers, 2014; Lavergne et al., 2019, 2020).

It follows that a global knowledge of internal tide lifecycle and a complete understanding of the various processes that impact their dynamics is required to better characterize the role of the internal tide in the ocean. This implies a quantification of the sources, sinks and energy pathways in between, of the internal tide. In situ observations can only provide limited information and cannot be used to reconstruct the whole lifecycle at large scales. On the other hand, maps of the low-mode internal tide distribution can be estimated using long-duration satellite altimeter data (Zaron, 2019; Zhao, 2018, 2019). However, they are restricted to the first two baroclinic modes and provide only rough estimates of the sources and sinks for the energy, with no further information on the physics behind. Numerical simulation thus stands out as an advantageous option for investigating the internal tide dynamics (Sarkar & Scotti, 2017). Indeed, several regional scale numerical studies of the internal tide dynamics have been previously performed (Kang & Fringer, 2012; Tchilibou et al., 2020; Zilberman et al., 2009). The past decade has seen the emergence of high resolution global numerical simulations that include internal tides (sometimes for the mere motivation that including internal tides would lead to a better solution compared to parameterizing their impact), which are used to characterize the internal tides field as well (Arbic et al., 2018; Savage et al., 2017; Z. Li et al., 2015). Numerical modeling of internal tides remains a numerically demanding and challenging task. One of the main reason is that the spectrum of internal waves spans a wide range of frequencies and wavelength, with the dissipation being driven by small scale processes such as shear and overturning instabilities (Sarkar & Scotti, 2017). As a result, internal tides can be sensitive to the numerical scheme and the various parameterization of the dissipation (Arbic et al., 2018). For instance, it has been shown that obtaining a realistic internal tide field in simulations with horizontal resolution of a few kilometers requires some tuning of the bottom drag (Buijsman et al., 2020).

In this study, we use a high-resolution numerical simulation to characterize the internal tide lifecycle over the North Mid-Atlantic ridge, in a domain centered around the Azores Islands. Our main motivation is to quantify the properties of the generation of the internal tide, its subsequent propagation and its dissipation. More precisely, we focus on the topographic scattering of internal tides: we show that it plays an important role in redistributing the energy among the vertical modes and, in the end, enhances dissipation in specific regions of the domain. Topographic scattering has been studied for several decades (Baines, 1971a, 1971b; Robinson, 1969), at the same time as early work on internal tide generation itself (by the barotropic tide), with special attention dedicated to its implication for mixing, especially near critical slopes (Gilbert & Garrett, 1989; Sarkar & Scotti, 2017). These studies mainly focused on describing the structure of the scattered tide over specific topographic profiles (usually along 2D vertical sections) and were later extended to random (Bühler & Holmes-Cerfon, 2011; Müller & Xu, 1992; Müller & Liu, 2000) and large amplitude topographies (Mathur et al., 2014; Y. Li & Mei, 2014). While the fundamental properties of topographic scattering are well captured by these theories, they also show that the solutions are too complicated to allow for an analytical resolution for general, realistic topographies (i.e., not simple isolated or statistically homogeneous profiles). This leaves room for numerical modeling based studies, and a large number of studies have been reported in the literature. However, most of the effort has been put around continental slopes (Griffiths & Grimshaw, 2007; Klymak et al., 2011, 2016; Kelly et al., 2012), where the internal tides are particularly intense and topographic scattering is a leading order process. Less attention has been dedicated to the global impact of topographic scattering in the deep ocean, over prominent features such as mid-ocean ridges. This study aims at addressing this issue by investigating topographic scattering, with the emphasis on its role for the internal tide lifecycle and its remote effects, in a region of the ocean with properties representative of mid-ocean ridges.

The rest of the study is organized as follows. First, in Section 2, we describe the numerical simulations which are used in the rest of the study, together with the linear theory relevant for their diagnostics. Then, a description of the internal tide lifecycle is given in Section 3, and the role of topographic scattering is discussed in Section 4. Finally, a discussion of the validity of the results in a realistic ocean, and comparison with theoretical expectations for the magnitude of topographic scattering, is given in Section 5. Section 6 concludes the study with a summary.

2. Methods

2.1. Linear Theory

Starting from the linearized Boussinesq equations, using barotropic/baroclinic decomposition (while retaining the free-surface condition) and averaging over tidal periods, one obtains the following equations for the vertically integrated baroclinic energy:

$$\frac{\partial}{\partial t}\left(\left\langle \frac{|\vec{v}|^2}{2} + \frac{b^2}{2N^2}\right\rangle\right) + \vec{\nabla} \cdot \vec{F}_{\text{bc}} = C_t - D, \tag{1}$$

where $\vec{v} = (u, v)$ is the baroclinic velocity, b the buoyancy anomaly, $N^2(z)$ is the horizontally homogeneous Brunt-Väisälä frequency and $\langle \ldots \rangle \equiv \int_{-H}^{0} \cdots \mathrm{d}z$ (with H the total fluid depth). The first term in Equation 1 is the tendency of the total (kinetic + potential) energy and the second term is the divergence of the energy flux $\vec{F}_{\text{bc}} = \langle \vec{v}p \rangle$, with p the baroclinic perturbation. Finally, the term C_t expresses the barotropic-to-baroclinic energy conversion and D the energy dissipation, as further discussed below.

Following a similar approach, one can use vertical normal modes to expand every variable (e.g., Gill, 1982; Wunsch, 2015). These normal modes are eigenvectors of a Sturm-Liouville problem (see A) and they arise by pair, one for example, the pressure—here denoted $\phi_n(z)$—and the other one for example, the vertical velocity. The modes are normalized here such that $\int_{-H}^{0} \phi_n\phi_m \mathrm{d}z = H\delta_{n,m}$, with $\delta_{n,m}$ the usual Kronecker delta symbol. Projecting the equations onto these modes gives a set of equations for the depth-integrated modal energy (Kelly et al., 2016):

$$H\frac{\partial}{\partial t}\left(\frac{|\vec{v}_n|^2}{2} + \frac{b_n^2}{2N^2}\right) + \vec{\nabla} \cdot \left(H\vec{v}_n p_n\right) = \sum_{m=0}^{N} C_{mn} - D_n, \tag{2}$$

where C_{mn} is the modal conversion term and $\vec{v}_n$, p_n, and b_n are the modal amplitude (projection) of the horizontal velocity, the pressure and the buoyancy, respectively.

The conversion term C_{mn} expresses the exchange of energy from mode m to mode n and reads (Kelly et al., 2012, 2016):

$$C_{mn} = p_n\vec{v}_m \cdot \int_{-H}^{0} \phi_m\vec{\nabla}\phi_n \mathrm{d}z - p_m\vec{v}_n \cdot \int_{-H}^{0} \phi_n\vec{\nabla}\phi_m \mathrm{d}z. \tag{3}$$

Note that the modes $\phi_n(z; \vec{x})$ depend on x, y in a parametric way, through their dependence on $H(x, y)$ and potentially to other environmental parameters (such as stratification). The total barotropic-to-baroclinic energy conversion is $C_t = \sum_n C_{0n}$, which simplifies under the rigid lid approximation to the well-known expression $C_t = -p(-H)\vec{V} \cdot \vec{\nabla}H$ (Llewellyn Smith & Young, 2002), where $\vec{V}$ is the barotropic velocity (i.e., $\vec{v}_0$).

The conversion terms C_{nm} involve horizontal derivatives, which make their numerical evaluation not convenient over varying bathymetry and with terrain-following vertical coordinates. To circumvent the horizontal derivatives and to clarify the physics behind the conversion term, we recast the latter using perturbation theory on the vertical modes, following Lahaye and Llewellyn Smith (2019). Assuming that the

stratification is horizontally homogeneous, as will be the case in most of the numerical simulations used in this study, and after some calculations (more details are given in A), we obtain the following equality:

$$\int_{-H}^{0} \phi_n \vec{\nabla} \phi_m \mathrm{d}z = \frac{\kappa_m^2}{\kappa_n^2 - \kappa_m^2} \phi_n \phi_m \mid_{-H} \vec{\nabla}H, \tag{4}$$

where κ_n is the eigenvalue associated with the vertical mode ϕ_n. This equation is then injected into Equation 3, leading to:

$$C_{mn} = \phi_n \phi_m \mid_{-H} \frac{\kappa_m^2 p_m \vec{u}_n - \kappa_n^2 p_n \vec{u}_m}{\kappa_n^2 - \kappa_m^2} \cdot \vec{\nabla}H. \tag{5}$$

This expression highlights the explicit, linear dependence of the magnitude of the energy scattering with the gradient of the topography.

In the energy balance equations depicted above (Equations 1 and 2), several processes were put aside, including nonlinear terms and interaction with the background current. Nonetheless, we can estimate an *a posteriori* dissipation of the internal wave by computing the difference between the conversion term and the left hand side of these equations. In the rest of the study, we will use the framework depicted above to diagnose the generation, scattering, and dissipation of internal tides in numerical simulations.

Using a weak-topography approximation, one can derive a linear solution to the barotropic modal conversion $C_n^{\mathrm{btrop}} \equiv C_{0n}$, as derived in Llewellyn Smith and Young (2002) and later implemented by Falahat et al. (2014) for global calculations. The barotropic modal conversion term (energy flux) is given by (e.g., Llewellyn Smith & Young, 2002):

$$C_n^{\mathrm{btrop}} = \rho_0 \frac{\phi_n^2|_{-H}}{8H} \frac{\omega^2 - f^2}{|\omega|} \iint_{x',y'} J_0\left(\kappa_n \left| \vec{x}' - \vec{x} \right|\right)$$
$$\left[U_0 \partial_x \partial_{x'} + U_0 V_0 \cos\chi \left(\partial_x \partial_{y'} + \partial_{x'} \partial_y \right) + V_0^2 \partial_y \partial_{y'} \right] H(\vec{x}) H(\vec{x}') \mathrm{d}^2 \vec{x}' \tag{6}$$

where κ_n is the modulus of the modal horizontal wavenumber (eigenvalue), the tidal barotropic current is $\left(U_0 \cos\left(\omega t + \varphi\right), V_0 \cos\left(\omega t + \varphi + \chi\right)\right)$ and J_0 is the Bessel function of the first kind. The different prefactor before the integral compared to Llewellyn Smith and Young (2002) is due to different normalization of the normal modes. Note that all the parameters ($\kappa_n, U_0, V_0, \varphi$, and χ as well as f) are functions of space, for example because of the large variations of depth. This dependence is not properly taken into account in the above approximate solution.

The total barotropic-to-baroclinic conversion term is formally given by $C_t = \sum\limits_n C_n^{\mathrm{btrop}}$. In practice, however, this infinite sum is approximated by taking the above equation in the limit of an infinite depth ocean, in which case the sum over the modes is replaced by an integral in the Fourier space (Llewellyn Smith & Young, 2002). The finite-depth effect is restored afterward by eliminating the contribution of waves having a vertical lengthscale larger than the depth of fluid (Nycander, 2005; Zilberman et al., 2009, and see Appendix B). In the rest of the study, our computation mostly follows the implementation of Zilberman et al. (2009) for the total, barotropic-to-baroclinic tidal conversion, and Falahat et al. (2014) for the modal conversion (see Appendix B).

2.2. Numerical Simulations

2.2.1. Numerical Setup

For the numerical simulation, we use the Coastal and Regional Ocean COmmunity model (CROCO), which is a branch from the Regional Oceanic Modeling System (Shchepetkin & McWilliams, 2005). It solves the hydrostatic primitive equations using terrain-following vertical coordinates. The numerical domain is a 1500 km wide square domain centered around the Azores Islands (see Figure 1b). The horizontal grid spacing is $dx = 750$ m, and there are 80 σ-levels refined near the surface and the bottom (with correspond-
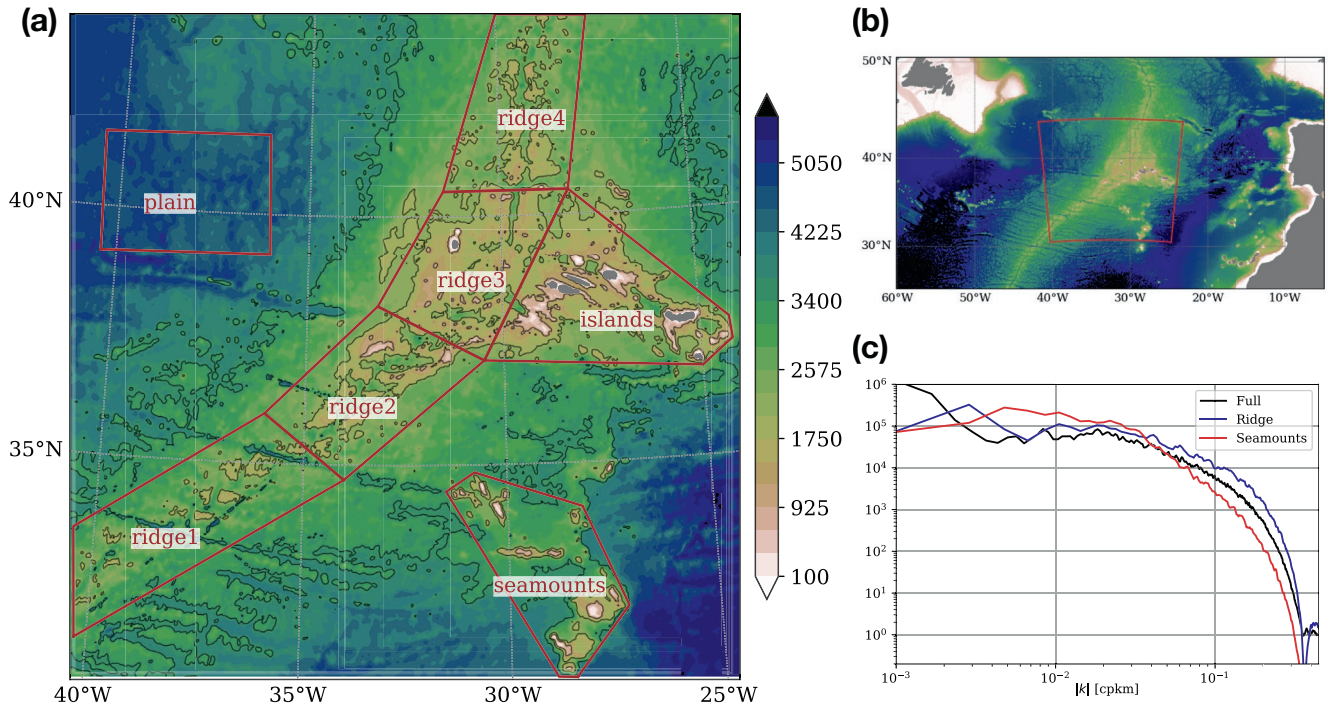
Figure 1. (a) Topography used in the numerical simulations. Subdomains of particular interest are superimposed in red contours. The Azores Islands are visible in the "Islands" subdomain, and the "seamounts" subdomain corresponds to the (northern part of the) Atlantis-Great Meteor Seamount Chain; (b) Bathymetry (from SRTM30_plus dataset) of a larger region of the North Atlantic, showing the location of the numerical domain; (c) Spectra of the topography (variance preserving) for the entire numerical domain and in two particular regions (square domains covering the "seamounts" and "ridge2" subdomains if (a))

ing stretching parameters $\theta_b = 4, \theta_s = 6$, and $h_c = 300$ m). We use open boundary conditions so that the generated internal tides leave the domain. A third order upstream-biased gradient operator is used (which is equivalent to a fourth order centered discretization and a bilaplacian viscosity). No explicit horizontal viscosity or diffusion is used. Vertical mixing is parameterized using KPP in the boundary layers (Large et al., 1994), and a Richardson-based criterion throughout the water column. A turbulent bottom drag parameterization is also used. Finally, the bathymetry is taken from the SRTM30plus dataset (Becker et al., 2009), with additional smoothing to limit discretization errors.

The configuration used in this study consists of a semi-realistic setup: the stratification is horizontally homogeneous, and its vertical profile is constructed by taking the horizontal mean stratification from an analogous simulation with a fully realistic configuration (Vic et al., 2018 and Section 5). Barotropic tidal forcing at the boundaries and tidal potential and self-attraction are taken respectively from TPXO7.2 and GOT99.2b. The numerical simulation is started at rest and only the M_2 component is forced. More details on the numerical setup can be found in Vic et al. (2018).

An *a priori* estimate of the number of vertical modes properly resolved in the numerical model can be obtained by comparing the grid point distribution with the mode structure. The eigenvalue κ further provides a local estimate of the horizontal wavelength of the internal waves. With our model configuration, the first 19 modes are well resolved along the horizontal, with at least four grid points per horizontal wavelength, throughout the domain, except in small shallower regions (small compared to the first baroclinic mode horizontal wavelength). In the vertical direction, modes up to $n = 10$ are resolved with more than three σ-levels between consecutive zeros (i.e., half-wavelength), and there is only one vertical level between consecutive zeros starting at mode number 19 over a significant portion of the domain (this coarser resolution occurs at middepth). We thus choose to truncate our modal analysis to mode number 19, which is only partially resolved, and often gather modes 10 to 19 in the diagnostics.

2.2.2. Bathymetry

Since internal tides are intrinsically linked to topography, we describe here the major topographic features of the region studied in the study. A map of the bathymetry used in the numerical simulation is shown in Figures 1a and 1b. The domain encompasses the Azores Triple Junction (at the intersection between the North American Plate, the Eurasian Plate, and the African Plate). The Mid Atlantic Ridge crosses the numerical domain from the southwest corner to the northern boundary, and the Azores Islands are visible in the eastern half of the domain, just above the middle latitude. In the southeastern sector of the domain, an ensemble of isolated seamounts are visible, which form the Seewarte Seamounts, also known as the Atlantis-Great Meteor Seamount Chain. However, the Great Meteor seamount, which is an identified hotspot of internal tide generation (e.g., Gerkema & van Haren, 2007; Kohler et al., 2019), is not included in the numerical domain.

The bathymetry is very variable in the domain considered, hosting islands, seamounts, and portions of abyssal plains deeper than 4,000 m at the southeastern and northwestern ends of the domain. In particular, the Seewarte Seamounts consist of isolated, large amplitude, and supercritical topographic features (with respect to the characteristic slope of semi-diurnal internal tide). The topography on the ridge itself consists of small scales topographic irregularities on top of more progressive large scale slopes. To illustrate this, the power spectral density of the topography is shown for these two distinct regions in Figure 1c: the variance at scales smaller than 10 km is about an order of magnitude larger on the ridge compared to the seamounts.

2.2.3. Diagnostics

The energy density and energy flux tendencies and divergence, as well as the conversion terms, are low-pass filtered using a fourth-order Butterworth filter (with typical cut-off period of 30 h) to obtain an estimate of the tidally averaged quantities. Prior to this, the variables entering the computation are bandpass filtered around the M_2 frequency (with a relative width of 1.2). This treatment does not alter the result significantly since the dynamics is greatly dominated by the M_2 tides. Any nonlinear effect that leads to tidal dissipation or transfer of energy to a frequency range out of the filtered band is included in the *a posteriori* estimated dissipation: this is virtually energy lost in a given frequency range.

3. Internal Tide Energy Cycle

3.1. Internal Tide Baroclinic Energy: Global View

The internal tide energetics is illustrated in Figure 2, where different quantities and terms from the balance Equation 1 for the vertically integrated baroclinic energy flux are shown. Topographic features are clearly distinguishable in every panel: the ridge crossing the domain, the isolated seamounts of the Atlantis-Meteor complex and the Azores archipelago. The last two topographic features can be identified as major sites for baroclinic tide generation by looking at the barotropic-to-baroclinic conversion term or the energy flux and its divergence (Figures 2a–2c). In contrast, the ridge is not a significant source of internal tides, except at a few narrow locations, showing patches of alternating signs for the energy flux divergence and the conversion term. In particular, no clear energy flux is measurable over the ridge. This is due to the fact that internal tides have a quite isotropic propagation direction here instead of being dominated by well-defined tidal beams. Moreover, the associated energy content is lower and/or more distributed over the highest part of the spectrum (modal energy flux scales like the modal energy density divided by the wavenumber). These aspects will be further discussed below.

After checking that the internal tide is in a quasistationary state (i.e., that the tendency of the low-pass filtered baroclinic tidal energy is negligible), we estimate the total energy dissipation following Equation 1 by computing $\vec{\nabla} \cdot \vec{F}_{bc} - C_t$. The result is shown in Figure 2e, and clearly exhibits hotspots of dissipation over the seamounts and near the islands, and over the shallowest parts of the ridge: most of the dissipation occurs in regions with depth smaller than 2,000 m. Negative dissipation value, in this estimate, may result from a residual error in the calculation of the different terms involved, or from neglected terms in the baroclinic energy Equation 1. The corresponding values remain small and are shaded in white in the Figure.
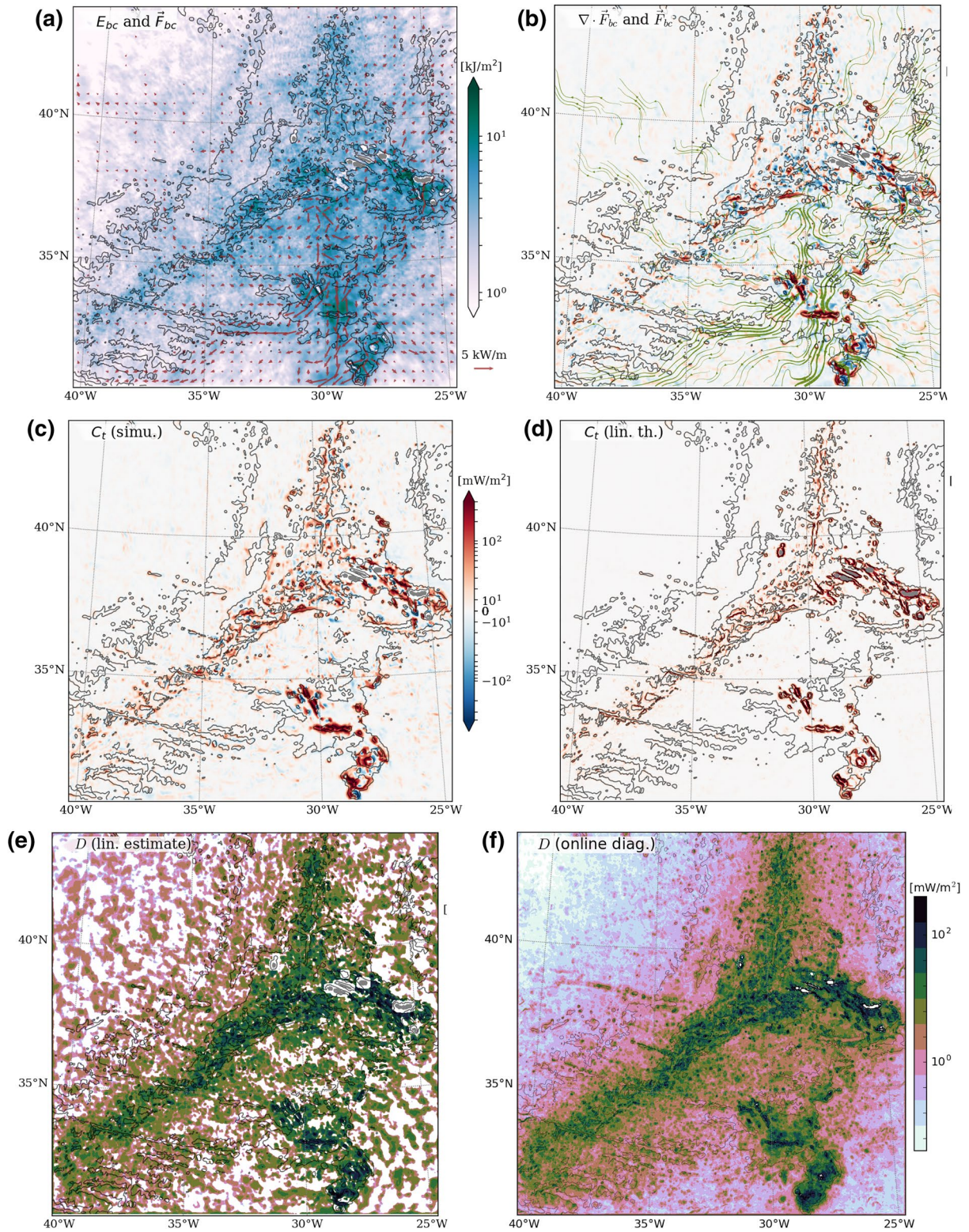
Figure 2. Energetics of the M_2 internal tide (vertically integrated): (a) Baroclinic energy (colors, log scale) and energy flux (arrows). (b) Divergence of the baroclinic energy flux (colors). A streamplot of the energy flux corresponding to the arrows in (a) is superimposed. (c and d) Barotropic-to-baroclinic conversion term C_t computed in the simulation and predicted by the linear solution, respectively. (e) Baroclinic energy dissipation inferred from the difference between the energy flux divergence and the conversion term (model estimate, negative values appears white—see text for explanation). (f) Total energy dissipation estimated from the model (online diagnostics). Plots with the same color scheme share the same colorbar.
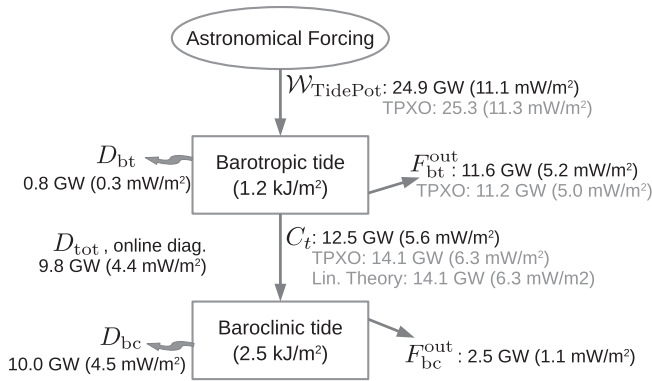
Figure 3. Energy pathways for the barotropic and baroclinic M_2 tide estimated from the numerical simulation: energy reservoirs (rectangles) and fluxes (arrows), integrated over the domain (and corresponding averages between parentheses). Estimates from TPXO8 and linear theory are indicated in gray when appropriate. Quantities below the barotropic tide energy reservoir correspond to the different terms of the vertically integrated baroclinic energy Equation 1. The tidal potential work $\mathcal{W}_{\text{TidePot}}$ is computed as the time average of $gH\vec{V} \cdot \vec{\nabla}P$, where P is the tidal potential.

This result can be compared with the total energy dissipation computed directly in the model (Figure 2f), which includes implicit diffusivity of the horizontal gradient operator, vertical mixing parameterizations and bottom drag. Here, the available potential energy (APE) dissipation is estimated taking advantage of the horizontal homogeneity of the background stratification, using a linear approximation to the APE (Kang & Fringer, 2010; Lamb, 2008; Roullet & Klein, 2009):

$$E_{ap} = \frac{1}{2} \frac{g^2 \rho'^2}{N^2}. \tag{7}$$

The online diagnostics is a measure of the total (barotropic + baroclinic) energy dissipation, although the fraction driven by the internal tide is dominant. Dissipation of the barotropic tide occurs through bottom drag. Both estimates of energy dissipation—based on linear theory, panel e and computed online in the model, panel f—show good qualitative agreement, especially above the ridge. Some discrepancies are visible over abyssal plains, although the dissipation is much weaker in these regions and could be related to nonlinear effects. In shallow region, the horizontal scales of internal waves decreases (for a given mode number and frequency) and reaches the limits of the model horizontal resolution. This could be responsible for enhanced dissipation, which should be kept in mind. Other mechanisms causing energy transfers within the internal wavefield and energy dissipation, such as nonlinear wave-wave interaction (including with the internal wave continuum, which is not present here), are likely to be underresolved in the numerical simulation (Arbic et al., 2018; Buijsman et al., 2017).

Finally, we compute the conversion term $Ct = \sum_n C_{0n}$ predicted by the linear theory (Equation 6), which depends on barotropic tidal currents and topography, for comparison with the model estimate, which uses the modeled baroclinic currents and pressure at the bottom (Equation 3). The corresponding maps are shown in Figures 2c and 2d respectively. Again, major hotspots of internal tide generation are discernible, and the global conversion rates (integrated over the entire domain where depth is greater than 300 m) with both methods show reasonable agreement: the linear calculation predicts 14 GW, while the model estimate gives 12.5 GW. However, a few striking differences appear. The conversion rate is much more positive all over the domain in the linear calculation, compared to the model estimate which exhibits regions with negative conversion. This is particularly remarkable over the ridge and in between the islands. Two major approximations used in the linear theory—besides linearity—are probably responsible for these discrepancies: (1) the weak-topography assumption, which is quite a crude approximation in regions with such large topographic variations, and (2) the way finite depth effects are taken into account in the computation of the linear solution. The latter indeed does not retain the discrete vertical modes, but use a high-pass spectral filter that aims at cutting modes with vertical wavelength larger than the local depth of fluid (see Appendix B and Nycander, 2005). Note that a negative conversion rate does not mean that energy is actually transferred from the baroclinic to the barotropic tide, but rather reflects the limitations in terms of physical meaning of the barotropic/baroclinic decomposition, which has often been debated (This confusion can be dispelled by averaging the conversion term in space, typically over patches larger than the first baroclinic mode lengthscale. Formally, only considering domains with boundaries passing through flat topography allows for clear-cut interpretation. Interesting examples of topographic features leading to baroclinic signatures locally while having zero net conversion can be found in Maas (2011)) (Gerkema, 2011; Kelly & Nash, 2011; Kelly et al., 2010).

To synthesize the global tidal energy path, a schematic in Figure 3 shows the energy transfers between the barotropic and the baroclinic tide, with sources (tidal potential) and sinks (dissipation) closing the budget. Estimates from TPXO8 are also indicated for comparison on the relevant quantities. We find that the corresponding values are close to our model estimates—although the presence of islands is likely a major source of errors.
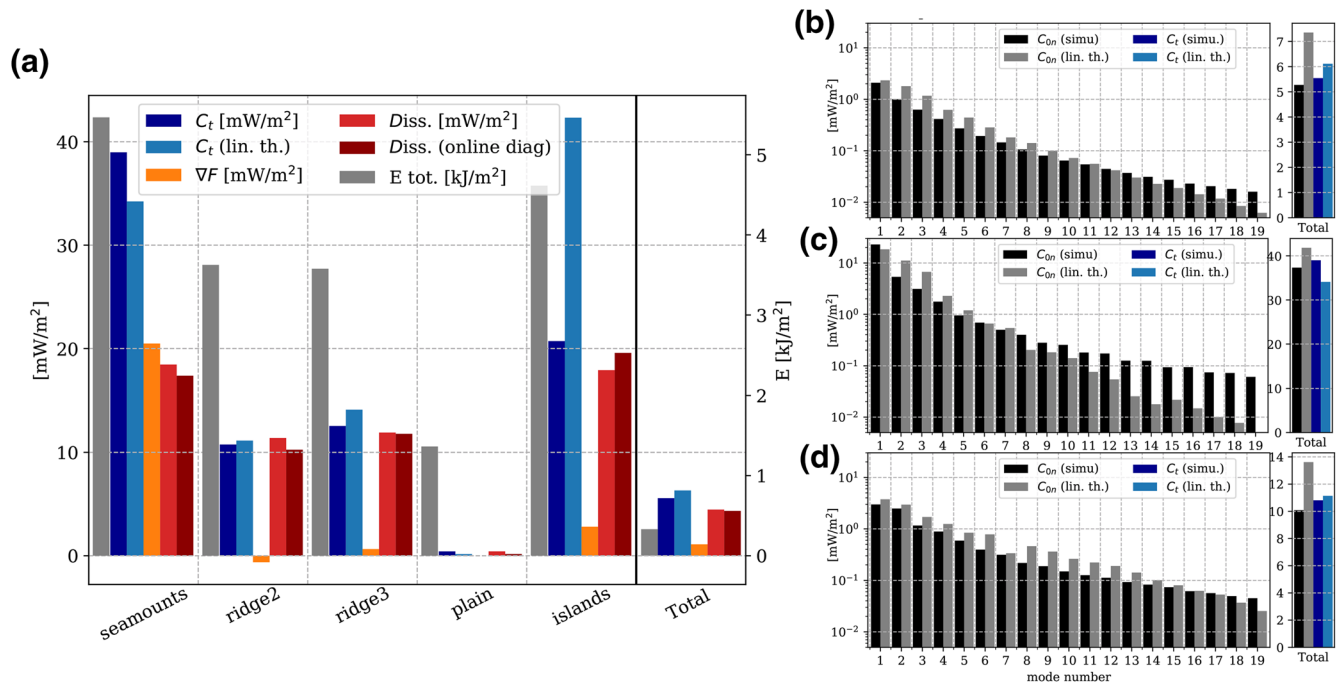
Figure 4. (a) Bar plot of the different terms of the vertically integrated baroclinic energy balance averaged in the subdomains depicted in Figure 1: Barotropic-baroclinic conversion term estimated in the model (dark blue) and from the linear solution (light blue), energy flux divergence (orange), energy dissipation estimate based on linear theory (baroclinic energy only, light red) and from online diagnostics (total energy, dark red); (b–d) Barotropic modal conversion rate: model estimate and linear theory, over the entire domain (b), the seamounts domain (c) and the "ridge2" domain (d).

3.2. Regional Characterization

As visible in Figure 2, the internal tide cycle exhibits contrasting properties over the region of interest. We now turn to a more quantitative discussion by looking at the different terms of the internal tide energy budget in the different domains introduced in Section 2.2 (Figure 1): several domains along the ridge, one over the Atlantis-Meteor complex, one over the abyssal plain in the North East and one around the Azores islands. We won't discuss in detail the energy cycle around the islands since it has a somewhat particular configuration (i.e., very shallow region), potentially associated with more important nonlinearities and numerical errors, and because the internal tide dynamics over such onshore region is not the focus of our study. The bar plot in Figure 4a shows the value of the vertically integrated energy density, the barotropic-to-baroclinic conversion term estimated from the model and using linear theory, the internal tide energy flux divergence and the estimated dissipation averaged over the different subdomains. Recall that an additional mask is used to ignore grid cells shallower than 300 m.

The overall agreement on the tidal conversion rate between linear theory and model estimate is good, although some discrepancies are visible when looking at particular regions. Indeed, linear theory has a tendency to underestimate the tidal conversion by the seamounts, while dramatically overestimating it around the islands. This is not surprising as the seamounts are characterized by very tall topographic features (with supercritical slopes) and, as mentioned previously, the islands subdomain is a very shallow region in which most of the assumptions of linear theory are inaccurate. However, the agreement between energy dissipation estimates based on the baroclinic energy linear balance (Equation 1) and the online diagnostics is rather good for all subdomains (as well as averaged over the full domain). Looking more closely at the generation per mode (Figures 4b–4d), it appears that linear theory overestimates the generation of lower modes while underestimating the generation of higher modes, in particular over the seamounts. As already mentioned in previous studies (e.g., Garrett & Kunze, 2007; Vic et al., 2019), regions populated with very steep topographic anomalies (such as the "seamounts" subdomain) have a steep spectrum (with respect to mode number), with large amplitude low modes being predominantly generated, while regions with smaller scale topographic features (such as the "ridge2" subdomain), have a shallower spectra. Interestingly, however,

this is more valid for the conversion rate predicted by linear theory (comparing gray bars in Figures 4c and 4d than what occurs in the model (black bars). Indeed, the latter exhibits a quite shallow spectrum for high wavenumbers (> 10). To our knowledge, this kind of disagreement between linear theory and numerical simulation has not been reported before in the literature.

The good agreement (excepted in the "Islands" subdomain) between quantities estimated from the model using the framework provided by linear theory, and the other estimates for the barotropic-to-baroclinic tidal conversion rate (from linear theory prediction) and most importantly online diagnostics of energy dissipation, is an indication that the above-mentioned framework is relevant for diagnosing the internal tide cycle in our study region. Only 20% of the generated internal tides leave the domain, the rest being dissipated inside the domain (Figure 4a). This fraction of locally dissipated energy is much smaller—50%—over the seamounts. In the even smaller domain enclosing the Plato seamount (a 1,000 m tall longitudinal ridge around ang30 W, ang33 N), this fraction goes down to 30%, which is a commonly assumed value for parametrization of internal tide induced energy dissipation (Garrett & Kunze, 2007) in global ocean models. In contrast, all over the ridge, the energy dissipation is roughly as important as the tidal conversion, meaning a nearly 100% local baroclinic tide dissipation fraction. In the "ridge2" domain, the net flux divergence is negative on average, meaning that the ridge dissipates more internal tide energy than it creates. The only possible explanation for such behavior is that internal tide energy coming from outside is dissipated inside this domain. As a result, while the ridge contributes weakly in internal tide generation compared to for example, the "seamounts" domain, it contributes significantly to the tidal energy dissipation, and thereby to the associated diapycnal mixing. Indeed, the mean value of C_t over the ridge is a quarter as large as in the "seamounts" domain, but the estimated dissipation is half as large. This shows that secondary processes leading to remote dissipation are important in this region.

4. Role of Internal Tide Scattering

In the previous section, we showed that the tidal energy cycle exhibits strong spatial variability, and that portions of the ridge are a net sink of internal tide energy. We inferred that secondary processes are important at least locally, among which topographic scattering is likely to be a dominant mechanism (the present numerical simulation does not have mesoscale turbulence). Topographic scattering consists of energy flux refraction and diffraction, the latter being associated with exchanges of energy between vertical modes. Since higher vertical modes are associated with relatively larger (vertical) shear, they enhance dissipation and mixing through shear instabilities and overturning. This is captured in the numerical model through the Richardson based vertical mixing parameterization. Hence, exchange of energy between modes likely plays a role in the dissipation rate of internal tides and thereby on the energy cycle of the internal tide. We thus investigate more closely the modal internal tide energy cycle, focusing on the topographic coupling. To do so, we use the modal energy Equation 2 that results from vertical mode decomposition of the linear equations. The barotropic modal conversion terms, as well as the scattering terms C_{mn} and the modal energy flux divergence, are computed in the different domains for the vertical modes up to $n = 19$. As in the previous section, we can infer a modal dissipation rate by taking the difference of the last two terms, since the tidal-averaged modal energy density is quasistationary.

4.1. Evidences of Topographic Scattering

We first discuss the results at the scale of the entire numerical domain, which are shown in Figure 5. The different terms are shown "per-mode" in panel a and cumulative over the modes in panel c. Slopes in panel c thus correspond to the bar height in panel a. The "scattering matrix" C_{mn} is shown in panel b, and the modal total baroclinic scattering:

$$C_{\text{bclin}}^n = \sum_{m \geq 1} C_{mn}$$

is further shown in panel a (note that $C_{nn} = 0$, as follows from Equation 3).
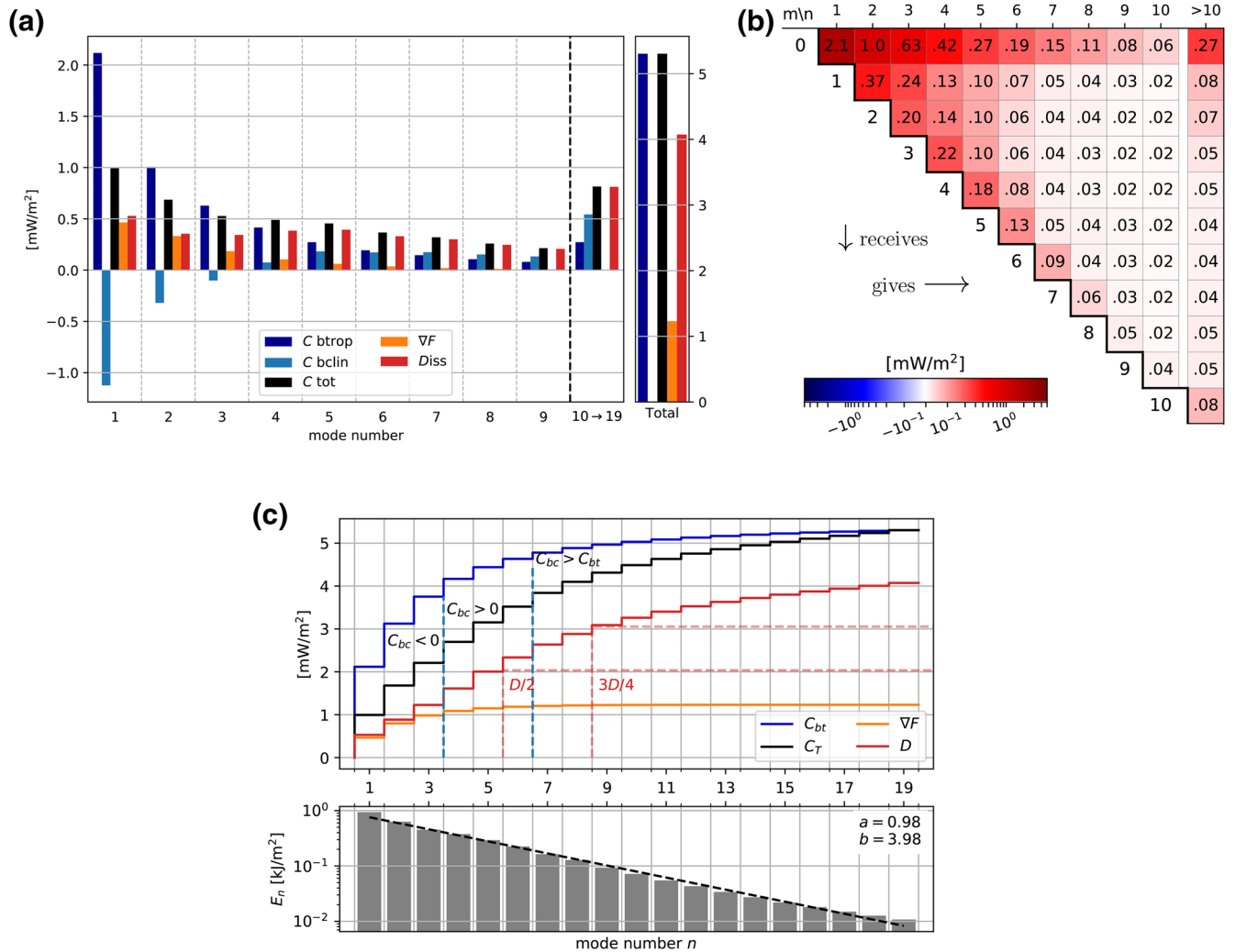
Figure 5. Internal tide scattering: (a) modal energy terms averaged over the entire numerical domain, with C_{bclin} the sum of the exchanges of one mode with every other baroclinic mode, that is, $C_{\text{bclin}}^n = \sum_{m>0} C_{mn}$; (b) matrix representation of the C_{mn} terms averaged in space. m (resp. n) increases with row (resp. column) number, and the first row corresponds to the barotropic-to-mode-n conversion term. Only the upper triangle is shown, as the matrix is antisymmetric. Energy exchanges with high modes (10 or 11 to 19) are gathered for clarity in (a) and (b). (c), upper panel: cumulative modal energy terms averaged over the same domain. The difference between the dark blue and the black curve is indicative of the redistribution among modes through baroclinic scattering. Regions where baroclinic scattering is negative, positive and greater than the barotropic conversion are indicated between these two curves. Also shown are typical fractions of total dissipation and corresponding mode number for which the partial cumulative modal dissipation reaches this value. (c), lower panel: mean modal energy density, with an exponential fit of the form $a\mathrm{e}^{-n/b}$ plotted in black dashed line.

Integrated over the domain, low modes (up to $n = 3$) loose a significant portion of their energy through scattering, while high modes ($n > 4$) gain energy through this process. For instance, the first baroclinic mode is generated by barotropic conversion at a rate slightly higher than 2mW / m², but only 0.4mW / m² leaves the domain, while 0.8mW / m² is transferred to higher modes and 0.8mW / m² is dissipated directly—mostly by the bottom drag—or transferred to vertical modes higher than $n = 19$ (which are not included in this analysis). The C_{mn} matrix provides a more detailed view of the baroclinic scattering process. The first line represents the barotropic modal conversion rate (i.e., the values correspond to the black bars in Figure 4a), which is higher than any baroclinic scattering term independently, given a "receiver" mode number n (i.e., column-wise). Topographic scattering globally consists of energy transfers to higher modes (all terms are positive), with higher rates for neighboring modes: the magnitude of the scattering indeed decreases with the difference of the mode numbers, that is, one mode n exchanges more energy with modes $n \pm 1$ than with modes $n \pm 2$ and so on. This confirms the recent analytic findings by Lahaye and Llewellyn Smith (2019):

they showed in a 2-dimensional $(x - z)$ domain, by combining the formula for the topographic scattering (Equation 5) and a Wentzel–Kramers–Brillouin-Jeffreys approximation for the vertical modes, that the magnitude of the topographic scattering is linearly proportional to the topography gradient and the inverse mode number difference.

The mean flux divergence rapidly goes to zero with increasing mode number, much faster than the net generation rate given by $C_n^{\text{btrop}} - C_n^{\text{bclin}}$ (Figures 5a and 5c). Thus, the high modes dissipate all their energy within the domain. As the scattering term increases with the mode number, while the barotropic modal conversion decreases, the former becomes dominant at a finite mode number, $n > 7$ in the present region. Thus, for higher wavenumbers, the input of energy by topographic scattering is the dominant mechanism of generation: the corresponding rate is more than twice the barotropic conversion for modes with $n \geq 10$.

This has potentially strong implications as high wavenumber internal tides are thought to play an important role in global dissipation and mixing in the ocean (Lefauve et al., 2015; Melet et al., 2013; Vic et al., 2019). In our case, mode numbers $n \geq 6$ account for half of the total energy dissipation. Our results evidence a cascade of energy toward higher modes—up to dissipation scales—where the exchange of energy is triggered by topographic scattering. It is one of the central results of this study. It further shows that this scattering can significantly contribute to the energy dissipated by the high wavenumber modes. Therefore, studies based solely on barotropic conversion linear calculations would likely miss an important part of the dissipation and associated mixing in some regions of the ocean by ignoring this component of the internal tide lifecycle.

4.2. Spatial Characterization of Scattering

We investigate the properties of topographic scattering in two regions with very different topography: the "seamounts" and "ridge2" subdomains (Figure 6).

Over the seamounts, baroclinic exchanges are relatively less active compared to over the ridge or over the entire domain. For high mode numbers, we even find negative (albeit weak) values, indicating higher to lower mode energy transfers.

The barotropic modal conversion term remains dominant at every mode number, and only the first mode loses energy through topographic scattering. The local mode 1 dissipation is only 17% of the barotropic generation and 25% of the net generation (barotropic conversion minus baroclinic scattering). These estimates do not take into account scattering to modes higher than $n = 20$, although these may be expected to be weak given the value of tidal scattering for modes $10 \leq n \leq 19$. The relatively small impact of baroclinic scattering and high modes in general is evidenced by the rather small differences between the net and the barotropic conversion rates (black and dark blue curves, respectively) as well as the dynamics of every curve, exhibiting rapid increase at small mode number and much shallower slopes at higher mode numbers (Figure 6a).

The picture is very different over the ridge: topographic scattering significantly redistributes the energy input by the barotropic tide, resulting in a much more progressive net conversion rate across mode numbers. Likewise, the modal dissipation is enhanced by high mode numbers, which explains why the dissipation is high over this region compared to the barotropic conversion, as mentioned previously—see Figure 4. For instance, the first baroclinic mode scatters to higher modes 90% of the input by the barotropic conversion and dissipates locally at a rate slightly larger than $1\text{mW} / \text{m}^2$. The latter is greater than the weak remaining net conversion, and is supplied by a net incoming flux through the boundaries of the domain of nearly $1\text{mW} / \text{m}^2$. This provides further explanation to the results discussed in the previous section, where we showed that this portion of the ridge is a sink for the internal tides. We now see that this segment receives energy carried by low modes entering from outside, that are dissipated—predominantly through topographic scattering to higher modes and also directly—within the domain, over the ridge.

Hence, the previous conclusions on the potential significance of topographic scattering for the tidally induced dissipation and mixing are further illustrated here, in a region representative of ocean ridges.
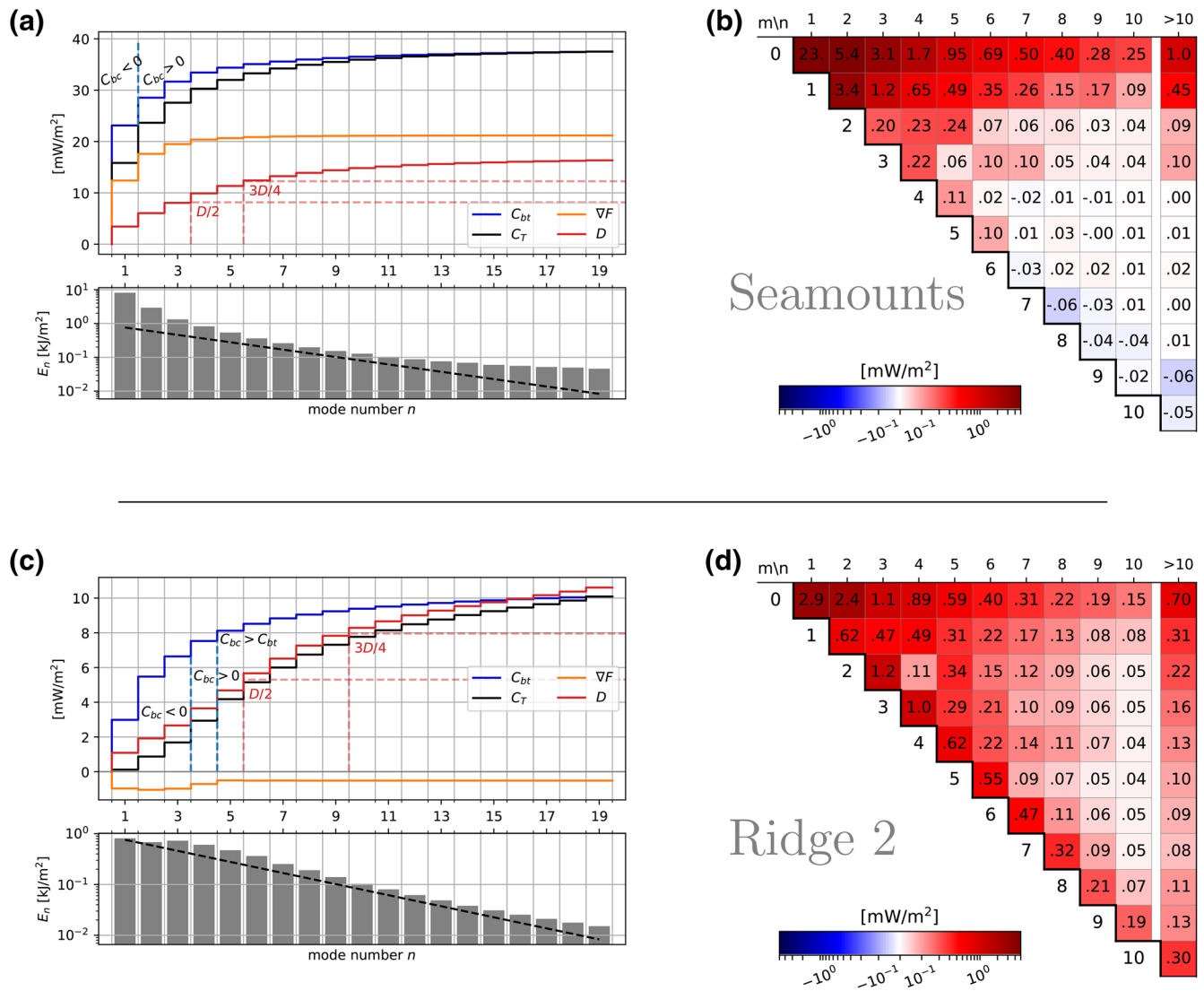
Figure 6. Same as Figures 5b and 5c, but for "seamounts" (top: (a) and (b) and "ridge2" (bottom: (c) and (d)) subdomains. Note that the extent of the vertical axis is different between (a) and (c). The black dashed curve in these panels (bottom frame) is the same as in Figure 5c for comparison.

5. Discussion

5.1. Extension to a Realistic Environment

The results presented so far were obtained in a numerical simulation with a semi-realistic configuration. It includes a realistic topography, but a mean horizontally homogeneous stratification and no background currents such as (sub)-mesoscale turbulence. It also included a single tidal component (M_2). Mesoscale turbulence is however present in the study region. For instance, it was recently investigated using the very same numerical setup with a focus on the deep currents (Vic et al., 2018; Lahaye, Gula, Thurnherr, et al., 2019) or on the surface signature of internal tides (Lahaye, Gula, & Roullet, 2019). Although investigating in detail the interaction between the balanced turbulence and the internal tides is beyond the scope of this study, we reproduced some of the diagnostics shown above that led to the main conclusions of the study in a fully realistic simulation, to check whether these results are applicable to a realistic ocean. The fully realistic simulation was constructed from a series of two nests, starting from a North-Atlantic basin-scale simulation (at 6 km resolution, see Gula et al., 2015) and using a "buffer" simulation of intermediate resolution ($dx = 2$ km). The one-way nesting approach uses the data from the latter at the boundaries of the present simulation
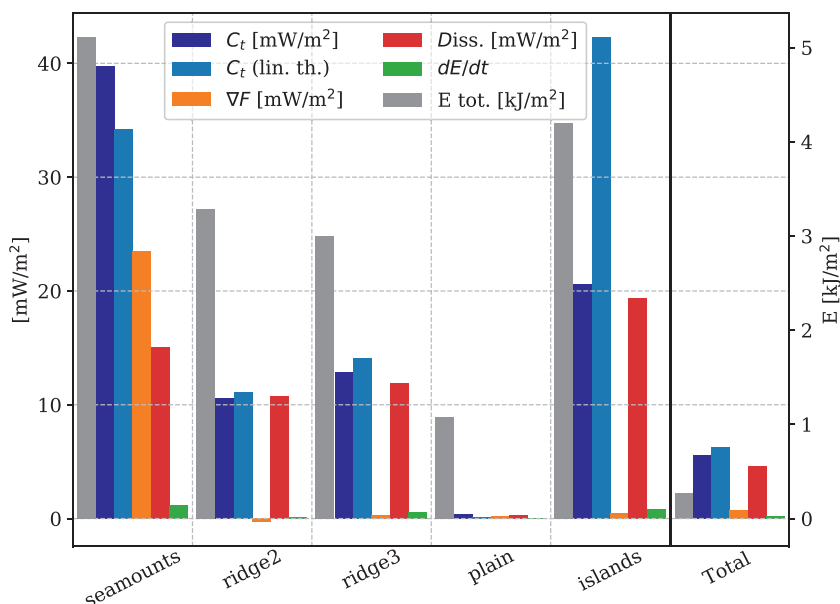
Figure 7. Vertically integrated baroclinic energy balance per subdomain (same as Figure 4, with online energy dissipation replaced by mean energy tendency) in the fully realistic simulation.

to force a realistic flow, that further develops into finer scale turbulence within the domain. Barotropic tidal forcing includes the eight most important components (four semi-diurnal and four diurnal). More details about the setup of the numerical simulation can be found in Vic et al. (2018) and Lahaye, Gula, Thurnherr, et al. (2019).

The theoretical framework for the analysis of these simulations is the same as described above. However, we do not use the online diagnostics of dissipation, as the computation of APE is more difficult in this realistic case and the aim of this study is not to quantify it precisely. We use a band-pass filter centered around the M_2 frequency, with a relative width of 1.2, to isolate the internal tide signal before computing the fluxes or performing the mode decomposition. For calculating the vertical modes, we computed a smoothed stratification using lowpass filtering in time and subsampling in space. Only the first 10 modes (including the barotropic mode) are computed. To take into account the spring neap cycle and additional variability associated with the different tidal components and the background turbulence, time average is performed over two periods of 15 days each: one in summer and one in winter. It should be mentioned that additional terms accounting for interactions between the background flow and the internal tides should be included in Equation 1 (Kang & Fringer, 2012), as well as in Equation 2 (but the latter is not used explicitly in what follows). These are not included in our diagnostics, which implies that our estimate of dissipation may contain some of these terms not accounted for, although we expect their importance to remain weak in this regions of moderate mesoscale activity and with the averaging procedure used here. The remainder of the variability due to the different tidal components in the forcing is subtracted from the baroclinic energy balance Equation 1 by removing the vertically integrated baroclinic energy density tendency over each time window (i.e., we do not use Equation 1 assuming a steady state any longer). Note that taking 15 days time averaging windows mostly remove the spring-neap cycle—as a result, the energy time tendency is small compared to the other terms.

The results of the baroclinic energy equation for the fully realistic simulation are given in Figure 7, which can be compared to the analogous figure in the semi-realistic configuration (Figure 4). Interestingly, the results remain very similar to the semi-realistic case. The only noticeable quantitative feature is the reduction of the dissipation in the seamounts subdomain (which could result from the neglected terms discussed above). It thus follows that the internal tide energy cycle is only weakly altered by the (sub)-mesoscale turbulence in this region. The topographic scattering was computed as previously and indeed shows the same quantitative features, that is, that there is a global transfer of energy from the smaller modes to the larger

Table 1
Decay Length Scale L_D (in km) and Time Scales τ_D (in Day) Estimated From the Theory and the Numerical Simulations, for the First baroclinic mode

Quantity \domain	Full	Ridge 2	Ridge 3	Seamounts	Plain
Theory: L_D	5787	249	347	657	6497
Numerics: L_D	794	287	250	381	9726
Numerics: τ_D	5.2	2.2	2.2	2.5	59
Numerics: τ_C	10.7	3.2	3.9	4.0	102
Numerics: τ_R	10.0	6.7	5.0	6.7	139

Note. Also given are the typical time scales associated with topographic scattering (τ_C) and with the residual dissipation (τ_R).

modes, which is more active over the ridge (not shown). Intercomparison of the periods used for the analysis however reveals interesting variability. In particular, one of the period exhibits weaker baroclinic scattering, which remains smaller than the barotropic conversion for every mode, even in the "ridge 2" subdomain. Correspondingly, the scattering matrices show inverse fluxes (negative values) on the first subdiagonal, that is, from a mode $n + 1$ to a mode n, while interactions between more distant modes (n to $n + 2$ and greater) remain globally positive, thus resulting in a decrease of the summed baroclinic scattering. The origin of this variability, which can be either due to the variability of the internal tide energy resulting from the barotropic forcing (mostly the spring neap cycle) or to interaction with the background flow, especially near the bottom (Lamb & Dunphy, 2018; Shakespeare & Hogg, 2019), would be worth investigating in a future study.

5.2. Comparison with Linear Theory

One motivation to this study is the possibility to capture and predict processes that affect the propagation of the internal tides—such as topographic scattering—for example, for the construction of accurate parameterization of the associated mixing for general circulation models (Eden & Olbers, 2014; Lavergne et al., 2020; MacKinnon et al., 2017). Analytical expectations have been derived using different approaches and assumptions (Buhler & Holmes-Cerfon, 2011; Y. Li & Mei, 2014), showing that the energy density of a given mode follows an exponential decay when passing over topographic irregularities with given statistical properties. The typical decay length scale λ depends on the latter: for instance Buhler and Holmes-Cerfon (2011) obtained the following equality (their Equation 5.4)

$$\lambda^{-1} = \frac{\pi \, \Gamma_0}{2H^2} \sqrt{\mathbf{E}\left|h\right|^2 \, \mathbf{E}\left|h'\right|^2}, \tag{8}$$

where h is the topographic deviation from the mean value H and h' its (one-dimensional) gradient. Γ_0 is a constant, which is fixed at $\sqrt{2\pi}$ following Lavergne et al. (2019). We constructed a map of the above quantity based on a local estimate of the topographic properties, computed in subdomains of size 100 km using a Hanning window, and averaged the result over the subdomains used throughout the study. This yields a theoretical prediction that we compare to similar estimates from the numerical simulation, computed as follows. From the modal energy balance, we define a typical decay time scale by dividing the (modal) energy dissipation by the (modal) energy density. Then, using the modal group velocity, a decay length scale is further constructed. These estimates are formed by first computing the spatial averages of the different quantities per subdomain, and then performing the division/multiplications.

The corresponding results, given in Table 1, exhibit overall a good agreement between the theoretical expectation and the evaluation in the numerical simulation. Typical decay time scales based on the baroclinic scattering rate and the residual dissipation (i.e., energy scattered to higher-than-computed modes or directly dissipated) are further provided for comparison. As expected, the shorter decay time and length scales are found over the ridge, while the largest ones are found over the abyssal plain. These results argue for using (and further developing) analytical estimates to account for topographic scattering of internal tides in reduced models of their propagation. As an additional remark, the exponential distribution that fits remarkably well with the modal energy averaged over the entire domain (Figure 5c) is an indication that simple scaling or results based on linear theory can indeed capture the mechanisms driving the internal tides.

6. Conclusion

The internal tide energy cycle and the importance of topographic scattering (exchange of energy between baroclinic modes) were investigated using regional numerical simulations at high resolution, with realistic (including (sub)-mesoscale turbulence) and semi-realistic (using a horizontally averaged stratification

profile) configurations. The region of interest, located over the North Mid-Atlantic Ridge around the Azores Islands, is representative of mid-ocean ridge systems. Mid-ocean ridges are known to play an important role in the global internal tide activity, and thereby on the ocean circulation through the impact of tides on diapycnal mixing.

The main results of this study can be summarized as follows:

- Internal tide generation and dissipation exhibit very different properties in different portions of the study regions
    - Isolated seamounts are responsible for most of the generation of internal tides, mainly of low vertical modes. Relative dissipation (dissipation/generation) is weaker there than the averaged value over the entire domain
    - In contrast, the ridge is a weak generator of internal tides. The modal distribution in this region is in favor of higher vertical modes, and the dissipation is around 100% of the generation. Some portions of the ridge dissipate more energy than they generate
- Topographic scattering leads to a forward cascade of energy from the lower modes to the higher modes, thereby enhancing dissipation. The corresponding flux of energy is greater than the barotropic conversion for vertical modes greater than six, globally
- Averaged over the entire domain, topographic scattering amounts to a cascade of energy between neighboring modes, which is more efficient for closest mode and fluxes toward higher modes
- The importance of topographic scattering is particularly high over the ridge, where it is responsible for scattering and dissipation of internal tides generated remotely

These results are important in the context of internal tide induced dissipation and mixing, and their parameterization for global ocean circulation models. It has been shown that remote effects, that is, processes involving long-range propagation of internal tides, bear large uncertainties and provide a significant proportion of internal tide dissipation, resulting in significant unknowns as far as its spatial distribution is concerned. Our results show that, among these processes, topographic scattering is indeed significant. In particular, it significantly enhances the transfer of energy to high vertical modes, which are known to play an important role for the internal tide dissipation, especially in the deep ocean. Our results show that the magnitude of topographic scattering is roughly captured by existing linear theory, supporting the use of parameterizations based on such theory. With this regard, it could be interesting to estimate the global contribution of internal tide scattering—beyond the first baroclinic mode, as previously studied by for example, Kelly et al. (2013)—, which is probably most conveniently available using a combination of tides-including global models and linear theory.

Other issues would be worth investigating as well, following the results presented in this study. For instance, the role of the mean flow in the processes highlighted here remains unclear. Our results exhibit moderate differences when mesoscale activity is included in the model. However, the study region is not a region of particularly intense turbulence and our diagnostics used average in time and in space. Nonstationarity of the internal tides were thus not investigated and left for future studies. In the light of recent work on the impact of mean flow over the barotropic-to-baroclinic tide conversion (Lamb & Dunphy, 2018; Shakespeare, 2020; Shakespeare & Hogg, 2019), and given the formal similarities between barotropic-to-baroclinic conversion and baroclinic scattering (Lahaye & Llewellyn Smith, 2019), mesoscale deep flow could lead to significant anisotropy in the topographic scattering process, which could in turn alter the impact of internal tides on the ocean circulation.

Appendix A: Vertical Modes and Perturbation Theory for Scattering Terms

The vertical modes are defined following the standard approach (e.g., Wunsch, 2015). For the reduced pressure $\phi = p / \rho_0$, the Sturm-Liouville eigenproblem is

$$\left(\frac{\phi_n'}{N^2}\right)' + \kappa_n^2\phi_n = 0, \quad \phi_n'(-H) = 0, \quad g\phi_n'(0) = -N^2(0)\phi_n(0) \tag{A1}$$

where prime denotes vertical derivative, N^2 is the Brunt-Väisälä frequency, g is gravity and κ_n the eigenvalue.

We now derive how perturbation theory can be used to recast variations of the vertical modes with space, resulting from variations of the topography, following Courant and Hilbert (1966); Lahaye and Llewellyn Smith (2019). We consider the eigenproblem with perturbed depth: $H \rightarrow H + \delta H$. Consequently, the eigenvalues and eigenfunctions are modified: $\kappa^2 \rightarrow \kappa^2 + \delta\kappa^2, \phi \rightarrow \phi + \delta\phi$ and are defined by the following equation (here written for a mode m):

$$\left(\frac{\phi_m{}' + \delta\phi_m{}'}{N^2} \right)' + \left(\kappa_m^2 + \delta\kappa_m^2 \right)\left(\phi_m + \delta\phi_m \right) = 0, \tag{A2}$$

which, retaining only the first order terms and subtracting Equation A1 with $n \rightarrow m$, gives

$$\left(\frac{\delta\phi_m{}'}{N^2} \right)' + \kappa_m^2 \delta\phi_m + \delta\kappa_m^2 \phi_m = 0. \tag{A3}$$

The corresponding boundary condition is unchanged at $z = 0$, and

$$\delta\phi_m{}' = \delta H \phi_m{}'', \quad \text{at} \quad z = -H$$

to ensure vanishing of the mode at $-\left(H + \delta H \right)$, at leading order in the perturbation.

We now project the perturbed Equation A3 on the basis of unperturbed modes by multiplying it by ϕ_n and integrating the result, which gives

$$\int\limits_{-H}^{0} \phi_n \left(\frac{\delta\phi_m{}'}{N^2} \right)' \mathrm{d}z + \kappa_m^2 \int\limits_{-H}^{0} \phi_n \delta\phi_m \mathrm{d}z + \delta\kappa_m{}^2 H \delta_{n,m} = 0, \tag{A4}$$

where the orthogonality condition $\int\limits_{-H}^{0} \phi_n \phi_m \mathrm{d}z = H \delta_{n,m}$ has been used. Integrating the first term by part twice and using the boundary conditions to get rid of the contributions at the boundaries in the second step gives

$$\int\limits_{-H}^{0} \phi_n \left(\frac{\delta\phi'_m}{N^2} \right)' \mathrm{d}z = -(\frac{\phi_n \delta\phi'_m}{N^2}|_{-H} - \kappa_n^2 \int\limits_{-H}^{0} \phi_n \delta\phi_m \mathrm{d}z$$

which can be injected into Equation A4 to obtain, for $n \neq m$

$$\int\limits_{-H}^{0} \phi_n \delta\phi_m \mathrm{d}z = -\frac{1}{\kappa_m^2 - \kappa_n^2} \frac{\phi_n \delta\phi_m{}'}{N^2} |_{-H} . \tag{A5}$$

The boundary condition for the perturbed mode is then used, as well as Equation A1 (for a mode m) evaluated at $z = -H$ (wherein $\left(\phi'_m / N^2 \right)' = \phi_m{}'' / N^2$ by virtue of the boundary condition for the unperturbed mode), to recast the r.h.s.~of the previous equation in terms of δH. In the case where variations in depth are caused by infinitely small displacement along the horizontal dimension (i.e., $\delta H = \vec{\nabla} H \cdot \vec{\delta x}$), one can use this result to express the horizontal derivative of the eigenmodes and obtain

$$\int\limits_{-H}^{0} \phi_n \vec{\nabla} \phi_m \mathrm{d}z = \frac{\kappa_m^2}{\kappa_n^2 - \kappa_m^2} \phi_n \phi_m |_{-H} \vec{\nabla} H, \tag{A6}$$

which is formally exact provided H is a continuous and differentiable function of space

Appendix B: Numerical Implementation of the Linear Calculation of the Conversion Terms

Modal Conversion C_{0n}

The linear prediction for the barotropic modal conversion shown in Figure 4 follows the method derived by Llewellyn Smith and Young (2002), resulting in the Equation 6, and the implementation of Falahat et al. (2014). Note that in this formulation, the barotropic tidal component as well as the vertical modes are assumed horizontally homogeneous, but nonhomogeneous fields are used in the computation. The barotropic tide data are taken from TPXO8 dataset. The topography as well as the stratification—and thereby the corresponding eigenmodes ϕ_n and eigenvalues κ_n—are taken from the numerical simulation. Unlike Falahat et al. (2014), however, we evaluate directly Equation 6, without using integration by parts and over the same grid as used in the CROCO simulations (i.e., without switching to tidal ellipse coordinates). To take into account horizontal variation of κ_n in the integral (resulting from variations of the topography), we evaluate the integral for several values of κ_n (typically, 10 per mode number) and interpolate linearly the result onto the local value of κ_n Contributions from regions shallower than 300 m are not taken into account.

Barotropic-To-Baroclinic Conversion Term C_t

The computation of the linear barotropic-to-baroclinic scattering term follows the implementation of Nycander (2005) and Zilberman et al. (2009). That is, the sum over an infinite number of vertical modes of C_n^{btrop} is replaced by a spectral integral over the continuous horizontal wavenumber $\vec{k} = (k, l)$ (infinite depth approximation), and the finite depth effect is approximated by using a high-pass spectral filter $g\left(\left|\vec{k}\right|\right)$ which suppresses contribution from unrealistic large wavelength. The conversion rate is thus given by Zilberman et al. (2009, their Equations A23–A25):

$$C\left(\vec{x}\right) = \frac{\rho_0 N_b}{2} \sqrt{1 - \frac{f^2}{\omega^2}} \left(\frac{\partial H}{\partial x} P_+\left(\vec{x}\right) + \frac{\partial H}{\partial y} P_-\left(\vec{x}\right) \right) \tag{B1}$$

with N_b the value of the Brunt-Väisälä frequency at the bottom, and where

$$P_+\left(\vec{x}\right) = U_0^2 \mathcal{F}^{-1}\left[\frac{ik}{\left|\vec{k}\right|} g\left(\left|\vec{k}\right|\right) \tilde{H} \right] + U_0 V_0 \cos \zeta \mathcal{F}^{-1}\left[\frac{il}{\left|\vec{k}\right|} g\left(\left|\vec{k}\right|\right) \tilde{H} \right] \tag{B2}$$

and P_- is similar to P_+ with $k \leftrightarrow l$ and $U_0 \leftrightarrow V_0$. Here, $\tilde{H}(k, l)$ is the Fourier transform of the (linearly detrended) topography. In our case, we use the (very simple) Heaviside step function for g, which discards contributions of wavenumbers below a threshold. The latter is taken as the mean mode 1 horizontal wavenumber, which is approximated based on the analytical solution for an exponential stratification that best fits the true $N(z)$ profile, following St. Laurent and Garrett (2002). The dataset used in this estimate are the same as for the modal conversion.

Data Availability Statement

Scripts used in this analysis, together with processed data and additional source files, can be obtained on the author's github (github.com/NoeLahaye/InTideScat_JGR).

References

Arbic, B. K., Alford, M. H., Ansong, J. K., Buijsman, M. C., Ciotti, R. B., Farrar, J. T., et al. (2018). Primer on global internal tide and internal gravity wave continuum modeling in HYCOM and MITgcm. In E. P. Chassignet, A. Pascual, J. Tintoré, & J. Verron (Eds.), *New Frontiers in Operational Oceanography* (pp. 307–392). GODAE OceanView. https://doi.org/10.17125/gov2018

Baines, P. G. (1971a). The reflexion of internal/inertial waves from bumpy surfaces. *Journal of Fluid Mechanics*, *46*(2), 273–291. https://doi.org/10.1017/S0022112071000533

Baines, P. G. (1971b). The reflexion of internal/inertial waves from bumpy surfaces. Part 2. Split reflexion and diffraction. *Journal of Fluid Mechanics*, *49*(1), 113–131. https://doi.org/10.1017/S0022112071001952

Baines, P. G. (1973). The generation of internal tides by flat-bump topography. *Deep-Sea Research and Oceanographic Abstracts*, *20*, 179–205.

Becker, J. J., Sandwell, D. T., Smith, W. H. F., Braud, J., Binder, B., Depner, J., et al. (2009). Global bathymetry and elevation data at 30 arc seconds resolution: SRTM30_PLUS. *Marine Geodesy*, *32*(4), 355–371. https://doi.org/10.1080/01490410903297766

Bell, T. H. (1975). Topographically generated internal waves in the open ocean. *Journal of Geophysical Research*, *80*(3), 320–327. https://doi.org/10.1029/JC080i003p00320

Bühler, O., & Holmes-Cerfon, M. (2011). Decay of an internal tide due to random topography in the ocean. *Journal of Fluid Mechanics*, *678*, 271–293. https://doi.org/10.1017/jfm.2011.115

Buijsman, M. C., Arbic, B. K., Richman, J. G., Shriver, J. F., Wallcraft, A. J., & Zamudio, L. (2017). Semidiurnal internal tide incoherence in the equatorial Pacific. *Journal of Geophysical Research: Oceans*, *122*(7), 5286–5305. https://doi.org/10.1002/2016JC012590

Buijsman, M. C., Stephenson, G. R., Ansong, J. K., Arbic, B. K., Green, J. A. M., Richman, J. G., et al. (2020). On the interplay between horizontal resolution and wave drag and their effect on tidal baroclinic mode waves in realistic global ocean simulations. *Ocean Modelling*, *152*, 101656. https://doi.org/10.1016/j.ocemod.2020.101656

Courant, R., & Hilbert, D. (1966). Methods of mathematical physics (Vol. 2). New York, NY: Intersience.

de Lavergne, C., Falahat, S., Madec, G., Roquet, F., Nycander, J., & Vic, C. (2019). Toward global maps of internal tide energy sinks. *Ocean Modelling*, *137*, 52–75. https://doi.org/10.1016/j.ocemod.2019.03.010

Duda, T. F., Lin, Y.-T., Buijsman, M., & Newhall, A. E. (2018). Internal tidal modal ray refraction and energy ducting in baroclinic gulf stream currents. *Journal of Physical Oceanography*, *48*(9), 1969–1993. https://doi.org/10.1175/JP0-D-18-0031.1

Dunphy, M., Ponte, A. L., Klein, P., & Le Gentil, S. (2017. March). Low-mode internal tide propagation in a turbulent Eddy field. *Journal of Physical Oceanography*, *47*(3), 649–665. https://doi.org/10.1175/JPO-D-16-0099.1

Eden, C., & Olbers, D. (2014). An energy compartment model for propagation, nonlinear interaction, and dissipation of internal gravity waves. *Journal of Physical Oceanography*, *44*(8), 2093–2106. https://doi.org/10.1175/JP0-D-13-0224.1

Falahat, S., Nycander, J., Roquet, F., & Zarroug, M. (2014). Global calculation of tidal energy conversion into vertical normal modes. *Journal of Physical Oceanography*, *44*(12), 3225–3244. https://doi.org/10.1175/JP0-D-14-0002.1

Franks, P. J. S., Garwood, J. C., Ouimet, M., Cortes, J., Musgrave, R. C., & Lucas, A. J. (2020). Stokes drift of plankton in linear internal waves: Cross-shore transport of neutrally buoyant and depth-keeping organisms. *Limnology and Oceanography*, *65*(6), 1286–1296. https://doi.org/10.1002/lno.11389

Garrett, C., & Kunze, E. (2007). Internal tide generation in the deep ocean. *Annual Review of Fluid Mechanics*, *39*(1), 57–87. https://doi.org/10.1146/annurev.fluid.39.050905.110227

Gerkema T. (2011). Comment on "Internal-tide energy over topography" by S. M. Kelly et al. *Journal of Geophysical Research*, *116*, (C7). http://dx.doi.org/10.1029/2010jc006611

Gerkema, T., & van Haren, H. (2007). Internal tides and energy fluxes over Great meteor seamount. *Ocean Science*, *9*, 441–449. https://doi.org/10.5194/os-3-441-2007

Gilbert, D., & Garrett, C. (1989). Implications for ocean mixing of internal wave scattering off irregular topography. *Journal of Physical Oceanography*, *19*(11), 1716–1729. https://doi.org/10.1175/1520-0485(1989)019(1716:IFOMOI)2.0.CO;2

Gill, A. E. (1982). Atmosphere-ocean dynamics (Vol. 30). Academic Press.

Griffiths, S. D., & Grimshaw, R. H. J. (2007). Internal tide generation at the continental shelf modeled using a modal decomposition: Two-dimensional results. *Journal of Physical Oceanography*, *37*(3), 428–451. https://doi.org/10.1175/JPO3068.1

Gula, J., Molemaker, M. J., & McWilliams, J. C. (2015). Gulf stream dynamics along the southeastern U.S. Seaboard. *Journal of Physical Oceanography*, *45*(3), 690–715. https://doi.org/10.1175/JPO-D-14-0154.1

Hennon, T. D., Alford, M. H., & Zhao, Z. (2019). Global assessment of semidiurnal internal tide aliasing in argo profiles. *Journal of Physical Oceanography*, *49*(10), 2523–2533. https://doi.org/10.1175/JPO-D-19-0121.1

Kafiabad, H. A., Savva, M. A. C., & Vanneste, J. (2019). Diffusion of inertia-gravity waves by geostrophic turbulence. *Journal of Fluid Mechanics*, *869*(R7), 1–13. https://doi.org/10.1017/jfm.2019.300

Kang, D., & Fringer, O. (2010). On the calculation of available potential energy in internal wave fields. *Journal of Physical Oceanography*, *40*(11), 2539–2545. https://doi.org/10.1175/2010JPO4497.1

Kang, D., & Fringer, O. (2012). Energetics of barotropic and baroclinic tides in the Monterey bay area. *Journal of Physical Oceanography*, *42*(2), 272–290. https://doi.org/10.1175/JPO-D-11-039.1

Kelly, S. M., Jones, N. L., Nash, J. D., & Waterhouse, A. F. (2013). The geography of semidiurnal mode-1 internal-tide energy loss. *Geophysical Research Letters*, *40*(17), 4689–4693. https://doi.org/10.1002/grl.50872

Kelly, S. M., Lermusiaux, P. F. J., Duda, T. F., Haley, J., & Patrick, J. (2016). A coupled-mode shallow-water model for tidal analysis: Internal tide reflection and refraction by the gulf stream. *Journal of Physical Oceanography*, *46*(12), 3661–3679. https://doi.org/10.1175/JPO-D-16-0018.1

Kelly, S. M., & Nash, J. D. (2011). Reply to comment by T. Gerkema on "Internal-tide energy over topography". *Journal of Geophysical Research*, *116*(C9). https://doi.org/10.1029/2011JC007040

Kelly S. M., Nash J. D., & Kunze E. (2010). Internal-tide energy over topography. *Journal of Geophysical Research*, *115*, (C6), http://dx.doi.org/10.1029/2009jc005618

Kelly, S. M., Nash, J. D., Martini, K. I., Alford, M. H., & Kunze, E. (2012). The cascade of tidal energy from low to high modes on a continental slope. *Journal of Physical Oceanography*, *42*(7), 1217–1232. https://doi.org/10.1175/JPO-D-11-0231.1

Klymak, J. M., Alford, M. H., Pinkel, R., Lien, R.-C., Yang, Y. J., & Tang, T.-Y. (2011). The breaking and scattering of the internal tide on a continen-al Slope. *Journal of Physical Oceanography*, *41*(5), 926–945. https://doi.org/10.1175/2010JP04500.1

Klymak, J. M., Simmons, H. L., Braznikov, D., Kelly, S., MacKinnon, J. A., Al-ford, M. H., et al. (2016). Reflection of linear internal tides from realistic topography: The Tasman continental slope. *Journal of Physical Oceanography*, *46*(11), 3321–3337. https://doi.org/10.1175/JP0-D-16-0061.1

Köhler, J., Walter, M., Mertens, C., Stiehler, J., Li, Z., Zhao, Z., et al. (2019). Energy flux observations in an internal tide beam in the eastern North Atlantic. *Journal of Geophysical Research: Oceans*, *124*(8), 5747–5764. https://doi.org/10.1029/2019JC015156

Kunze, E. (2017a). The internal-wave-driven meridional overturning circulation. *Journal of Physical Oceanography*, *47*(11), 2673–2689. https://doi.org/10.1175/JP0-D-16-0142.1

Kunze, E. (2017b). Internal-wave-driven mixing: Global geography and bud-gets. *Journal of Physical Oceanography*, *47*(6), 1325–1345. https://doi.org/10.1175/JP0-D-16-0141.1

Lahaye, N., Gula, J., & Roullet, G. (2019). Sea surface signature of internal tides. *Geophysical Research Letters*, *46*(7), 3880–3890. https://doi.org/10.1029/2018GL081848

Lahaye, N., Gula, J., Thurnherr, A. M., Reverdin, G., Bouruet-Aubertot, P., & Roullet, G. (2019). Deep currents in the Rift valley of the north mid-Atlantic ridge. *Frontiers in Marine Science*, *6*(597), 1–17. https://doi.org/10.3389/fmars.2019.00597

Lahaye, N., & Llewellyn Smith, S. G. (2019). Modal analysis of internal wave propagation and scattering over large-amplitude topography. *Journal of Physical Oceanography*, *50*(2), 305–321. https://doi.org/10.1175/JP0-D-19-0005.1

Lamb, K. G. (2008). On the calculation of the available potential energy of an isolated perturbation in a density-stratified fluid. *Journal of Fluid Mechanics*, *597*, 415–427. https://doi.org/10.1017/S0022112007009743

Lamb, K. G. (2014). Internal wave breaking and dissipation mechanisms on the continental slope/shelf. *Annual Review of Fluid Mechanics*, *46*(1), 231–254. https://doi.org/10.1146/annurev-fluid-011212-140701

Lamb, K. G., & Dunphy, M. (2018). Internal wave generation by tidal flow over a two-dimensional ridge: Energy flux asymmetries induced by a steady surface trapped current. *Journal of Fluid Mechanics*, *836*, 192–221. https://doi.org/10.1017/jfm.2017.800

Large, W. G., McWilliams, J. C., & Doney, S. C. (1994). 0ceanic vertical mixing: A review and a model with a nonlocal boundary layer parameterization. *Reviews of Geophysics*, *32*(4), 363. https://doi.org/10.1029/94RG01872de

Lavergne, C., Vic, C., Madec, G., Roquet, F., Waterhouse, A. F., Whalen, C. B., et al. (2020). A parameterization of local and remote tidal mixing. *Journal of Advances in Modeling Earth Systems*, *12*(5), e2020MS002065. https://doi.org/10.1029/2020MS002065

Lefauve, A., Muller, C., & Melet, A. (2015). A three-dimensional map of tidal dissipation over abyssal hills. *Journal of Geophysical Research: Oceans*, *120*(7), 4760–4777. https://doi.org/10.1002/2014JC010598

Li, Y., & Mei, C. C. (2014). Scattering of internal tides by irregular bathymetry of large extent. *Journal of Fluid Mechanics*, *747*, 481–505. https://doi.org/10.1017/jfm.2014.159

Li, Z., von Storch, J.-S., & Müller, M. (2015). The M2 internal tide simulated by a 1/10° OGCM. *Journal of Physical Oceanography*, *45*(12), 3119–3135. https://doi.org/10.1175/JP0-D-14-0228.1

Li, B., Wei, Z., Wang, X., Fu, Y., Fu, Q., Li, J., & Lv, X. (2020). Variability of coherent and incoherent features of internal tides in the north South China Sea. *Scientific Reports*, *10*(1), 12904. https://doi.org/10.1038/s41598-020-68359-7

Llewellyn Smith, S. G., & Young, W. (2002). Conversion of the barotropic tide. *Journal of Physical Oceanography*, *32*(5), 1554–1566.

Maas, L. R. M. (2011). Topographies lacking tidal conversion. *Journal of Fluid Mechanics*, *684*, 5–24. https://doi.org/10.1017/jfm.2011.245

MacKinnon, J. A., Alford, M. H., Sun, O., Pinkel, R., Zhao, Z., & Klymak, J. (2012). Parametric subharmonic instability of the internal tide at 29°N. *Journal of Physical Oceanography*, *43*(1), 17–28. https://doi.org/10.1175/JP0-D-11-0108.1

MacKinnon, J. A., Zhao, Z., Whalen, C. B., Waterhouse, A. F., Trossman, D. S., Sun, O. M., et al. (2017). Climate process team on internal wave-driven ocean mixing. *Bulletin of the American Meteorological Society*, *98*(11), 2429–2454. https://doi.org/10.1175/BAMS-D-16-0030.1

Mathur, M., Carter, G. S., & Peacock, T. (2014). Topographic scattering of the low-mode internal tide in the deep ocean. *Journal of Geophysical Research: Oceans*, *119*(4), 2165–2182. https://doi.org/10.1002/2013JC009152

McComas, C. H., & Bretherton, F. P. (1977). Resonant interaction of oceanic internal waves. *Journal of Geophysical Research*, *82*(9), 1397–1412. https://doi.org/10.1029/JC082i009p01397

Melet, A., Hallberg, R., Legg, S., & Polzin, K. (2012). Sensitivity of the ocean state to the vertical distribution of internal-tide-driven mixing. *Journal of Physical Oceanography*, *43*(3), 602–615. https://doi.org/10.1175/JPO-D-12-055.1

Melet, A., Legg, S., & Hallberg, R. (2016). Climatic impacts of parameterized local and remote tidal mixing. *Journal of Climate*, *29*(10), 3473–3500. https://doi.org/10.1175/JCLI-D-15-0153.1

Melet, A., Nikurashin, M., Muller, C., Falahat, S., Nycander, J., Timko, P. G., et al. (2013). Internal tide generation by abyssal hills using analytical theory. *Journal of Geophysical Research: Oceans*, *118*(11), 6303–6318. https://doi.org/10.1002/2013JC009212

Müller, P., & Xu, N. (1992). Scattering of oceanic internal gravity waves off random bottom topography. *Journal of Physical Oceanography*, *22*(5), 474–488. https://doi.org/10.1175/1520-0485(1992)022(0474:SOOIGW)2.0.CO;2

Müller, P., Holloway, G., Henyey, F., & Pomphrey, N. (1986). Nonlinear interactions among internal gravity waves. *Reviews of Geophysics*, *24*(3), 493–536. https://doi.org/10.1029/RG024i003p00493

Müller, P., & Liu, X. (2000). Scattering of internal waves at finite topography in two dimensions. Part I: Theory and case studies. *Journal of Physical Oceanography*, *30*, 18.

Morrow, R., Fu, L.-L., Ardhuin, F., Benkiran, M., Chapron, B., Cosme, E., et al. (2019). Global observations of fine-scale ocean surface topography with the surface water and ocean topography (SWOT) mission. *Frontiers in Marine Science*, *6*(332). https://doi.org/10.3389/fmars.2019.00232

Nash, J. D., Kelly, S. M., Shroyer, E. L., Moum, J. N., & Duda, T. F. (2012). The unpredictable nature of internal tides on continental shelves. *Journal of Physical Oceanography*, *42*(11), 1981–2000. https://doi.org/10.1175/JPO-D-12-028.1

Nelson, A. D., Arbic, B. K., Zaron, E. D., Savage, A. C., Richman, J. G., Buijsman, M. C., & Shriver, J. F. (2019). Toward realistic nonstationarity of semidiurnal baroclinic tides in a hydrodynamic model. *Journal of Geophysical Research: Oceans*, *124*(9), 6632–6642. https://doi.org/10.1029/2018JC014737

Nycander J. (2005). Generation of internal waves in the deep ocean by tides. *Journal of Geophysical Research*, *110*(C10). https://doi.org/10.1029/2004jc002487

Olbers, D. J. (1976). Nonlinear energy transfer and the energy balance of the internal wave field in the deep ocean. *Journal of Fluid Mechanics*, *74*(2), 375–399. https://doi.org/10.1017/S0022112076001857

Olbers, D., Pollmann, F., & Eden, C. (2019). On PSI interactions in internal gravity wave fields and the decay of baroclinic tides. *Journal of Physical Oceanography*, *50*(3), 751–772. https://doi.org/10.1175/jpo-d-19-0224.1

Onuki, Y., & Hibiya, T. (2018). Decay rates of internal tides estimated by an improved wave-wave interaction analysis. *Journal of Physical Oceanography*, *48*(11), 2689–2701. https://doi.org/10.1175/JPO-D-17-0278.1

Pairaud, I. L., Auclair, F., Marsaleix, P., Lyard, F., & Pichon, A. (2010). Dynamics of the semi-diurnal and quarter-diurnal internal tides in the Bay of Biscay. Part 2: Baroclinic tides. *Continental Shelf Research*, *30*(3), 253–269. https://doi.org/10.1016/j.csr.2009.10.008

Polzin, K. L., & Lvov, Y. V. (2011). Toward regional characteriza-tions of the oceanic internal wavefield. *Reviews of Geophysics*, *49*(4), RG4003. https://doi.org/10.1029/2010RG000329

Polzin, K. L., Toole, J. M., Ledwell, J. R., & Schmitt, R. W. (1997). Spatial variability of turbulent mixing in the abyssal ocean. *Science*, *276*(5309), 93–96. https://doi.org/10.1126/science.276.5309.93

Ponte, A. L., Klein, P., Dunphy, M., & Le Gentil, S. (2017). Low-mode internal tides and balanced dynamics disentanglement in altimetric observations: Synergy with surface density observations. *Journal of Geophysical Research: Oceans*, *122*(3), 2143–2155. https://doi.org/10.1002/2016JC012214

Qiu, B., Nakano, T., Chen, S., & Klein, P. (2017). Submesoscale transition from geostrophic flows to internal waves in the northwestern Pacific upper ocean. *Nature Communications*, *8*, 14055. https://doi.org/10.1038/ncomms14055

Robinson, R. (1969). The effects of a vertical barrier on internal waves. *Deep-Sea Research and Oceanographic Abstracts*, *16*(5), 421–429. https://doi.org/10.1016/0011-7471(69)90030-8

Roullet, G., & Klein, P. (2009). Available potential energy diagnosis in a direct numerical simulation of rotating stratified turbulence. *Journal of Fluid Mechanics*, *624*, 45–55. https://doi.org/10.1017/S0022112008004473

Sarkar, S., & Scotti, A. (2017). From topographic internal gravity waves to turbulence. *Annual Review of Fluid Mechanics*, *49*(1), 195–220. https://doi.org/10.1146/annurev-fluid-010816-060013

Savage, A. C., Arbic, B. K., Alford, M. H., Ansong, J. K., Farrar, J. T., Menemenlis, D., et al. (2017). Spectral decomposition of internal gravity wave sea surface height in global models. *Journal of Geophysical Research: Oceans*, *122*(10), 7803–7821. https://doi.org/10.1002/2017JC013009

Savva, M. A. C., & Vanneste, J. (2018). Scattering of internal tides by barotropic quasigeostrophic flows. *Journal of Fluid Mechanics*, *856*, 504–530. https://doi.org/10.1017/jfm.2018.694

Shakespeare, C. J. (2020). Interdependence of internal tide and lee wave generation at abyssal hills: Global calculations. *Journal of Physical Oceanography*, *50*(3), 655–677. https://doi.org/10.1175/jpo-d-19-0179.1

Shakespeare, C. J., & McC. Hogg, A. (2019). On the momentum flux of internal tides. *Journal of Physical Oceanography*, *49*(4), 993–1013. https://doi.org/10.1175/jpo-d-18-0165.1

Sharples, J., Moore, C. M., Hickman, A. E., Holligan, P. M., Tweddle, J. F., Palmer, M. R., & Simpson, J. H. (2009). Internal tidal mixing as a control on continental margin ecosystems. *Geophysical Research Letters*, *36*(23). https://doi.org/10.1029/2009gl040683

Shchepetkin, A. F., & McWilliams, J. C. (2005). The regional oceanic modeling system (ROMS): A split-explicit, free-surface, topography-following-coordinate oceanic model. *Ocean Modelling*, *9*(4), 347–404. https://doi.org/10.1016/j.ocemod.2004.08.002

St. Laurent, L., & Garrett, C. (2002). The role of internal tides in mix-ing the deep ocean. *Journal of Physical Oceanography*, *32*(10), 2882–2899. https://doi.org/10.1175/1520-0485(2002)032⟨2882:TR0ITI⟩2.0.C0;2

Tchilibou, M., Gourdeau, L., Lyard, F., Morrow, R., Koch Larrouy, A., Allain, D., & Djath, B. (2020). Internal tides in the Solomon Sea in contrasted ENSO conditions. *Ocean Science*, *16*(3), 615–635. https://doi.org/10.5194/os-16-615-2020

Torres, H. S., Klein, P., Menemenlis, D., Qiu, B., Su, Z., Wang, J., et al. (2018). Partitioning ocean motions into balanced motions and internal gravity waves: A modeling study in anticipation of future space missions. *Journal of Geophysical Research: Oceans*, *123*(11), 8084–8105. https://doi.org/10.1029/2018JC014438

Tuerena, R. E., Williams, R. G., Mahaffey, C., Vic, C., Green, J. A. M., Naveira- Garabato, A., et al. (2019). Internal tides drive nutri-ent fluxes into the deep chlorophyll maximum over mid-ocean ridges. *Global Biogeochemical Cycles*, *33*(8), 995–1009. https://doi.org/10.1029/2019GB006214

Vic, C., Gula, J., Roullet, G., & Pradillon, F. (2018). Dispersion of deep-sea hy-drothermal vent effluents and larvae by submesoscale and tidal currents. *Deep Sea Research Part I: Oceanographic Research Papers*, *133*, 1–18. https://doi.org/10.1016/j.dsr.2018.01.001

Vic, C., Naveira Garabato, A. C., Green, J. A. M., Waterhouse, A. F., Zhao, Z., Melet, A., et al. (2019). Deep-ocean mix-ing driven by small-scale internal tides. *Nature Communications*, *10*(1), 2099. https://doi.org/10.1038/s41467-019-10149-5

Wunsch, C. (1975). Internal tides in the ocean. *Reviews of Geophysics*, *13*(1), 167. https://doi.org/10.1029/RG013i001p00167

Wunsch, C. (2015). *Modern observational physical oceanography*. Princeton and Oxford: Princeton University Press. Retrieved from https://press.princeton.edu/books/hardcover/9780691158822/modern-observational-physical-oceanography

Zaron, E. D. (2019). Baroclinic tidal sea level from exact-repeat mission altimetry. *Journal of Physical Oceanography*, *49*(1), 193–210. https://doi.org/10.1175/JPO-D-18-0127.1

Zhao, Z. (2018). The global mode-2 M2 internal tide. *Journal of Geophysical Research: Oceans*, *123*(11), 7725–7746. https://doi.org/10.1029/2018JC014475

Zhao, Z. (2019). Mapping internal tides from satellite altimetry without blind directions. *Journal of Geophysical Research: Oceans*, *124*(12), 8605–8625. https://doi.org/10.1029/2019jc015507

Zilberman, N. V., Becker, J. M., Merrifield, M. A., & Carter, G. S. (2009). Model estimates of M2 internal tide generation over mid- Atlantic ridge topography. *Journal of Physical Oceanography*, *39*(10), 2635–2651. https://doi.org/10.1175/2008JPO4136.1